RSC Applied Interfaces

ROYAL SOCIETY OF CHEMISTRY

PAPER

View Article Online
View Journal | View Issue

Cite this: *RSC Appl. Interfaces*, 2025, **2**, 1631

Facet- and graphene-support-dependent activity of Ta_2O_5 for oxygen evolution reaction

Ebrahim Ghasemy, Ana C. Tavares* and Kulbir K. Ghuman *

Received 15th July 2025,
Accepted 12th September 2025

DOI: 10.1039/d5lf00195a

rsc.li/RSCApplInter

Ta_2O_5 is among the few metal oxides that are stable in acidic media but, due to its insulating nature, its use in electrocatalytic oxygen evolution reaction (OER) has been less explored. Herein, density functional theory calculations were performed on three different Ta_2O_5 facets, pristine and with O or Ta defects. The goal was to identify strategies to improve the OER performance of Ta_2O_5 by establishing correlations with its intrinsic properties. The study revealed that the OER activity of Ta_2O_5 is facet-dependent according to the following trend (200) > (120) > (001), which correlated with the Ta density on the topmost atomic layer. The lowest overpotential, 0.61 V, was observed at the Ta–O site of the pristine (200) facet, followed by a Ta site on the same facet with a Ta defect (0.63 V). The moderate density of states (DOS) at the Fermi level and lower Ta site density on the (200) surface contributed to its higher performance compared to other facets. The correlation analysis conducted by considering Bader charge, d-band analysis of Ta sites, and valence electrons showed strong correlations for (120) surfaces, whereas (200) surfaces had moderate correlations. As a conductive phase is often added to insulating materials in experiments, the (200) Ta_2O_5/graphene heterostructure was also studied. An overpotential as low as 0.39 V was found for the Ta–O sites of the heterostructure. According to the partial DOS analysis, the improved OER performance of the heterostructure can be attributed to the shift in the d orbitals of Ta sites toward lower energies and the increase in the DOS intensity. This study offers valuable insights for designing Ta_2O_5-based electrocatalysts for OER in acidic media.

1. Introduction

As a carbon-free energy vector, green hydrogen can enable clean electricity production, helping to meet the targets for reducing the emission of greenhouse gases (GHGs).[1] It has been estimated that green hydrogen can reduce CO_2 emissions by six gigatonnes and meet 18% of energy demands.[2,3] According to the hydrogen strategy for Canada, clean hydrogen is capable of delivering 30% of end-use energy in the country by 2050, reducing the emission of CO_2 by up to 190 Mt.[4] When powered by electricity from renewable sources, water electrolyzers can sustainably produce green hydrogen.[5] This process involves two reactions, *i.e.*, hydrogen evolution reaction (HER) and oxygen evolution reaction (OER) on the cathode and anode, respectively. However, the hydrogen production cost through hydrolysis (considering electricity cost of 5 cents US$ per kW h) is twice the H_2 production methods based on natural gas.[6]

OER is a sluggish reaction that includes four electron-proton transfer steps and requires a high overpotential.[7–10] Proton exchange membrane water electrolyzers (PEMWEs) that work in an acidic environment are superior to alkaline electrolysis technologies. This is because PEMWEs have higher efficiency, higher production rates per unit electrode area, faster electrode kinetics, and a more compact design.[11] The best OER electrocatalysts are based on Ru and Ir materials, with Ru-based materials having higher OER activity but weaker stability compared to Ir-based materials.[12] The high cost and scarcity of these catalysts increase the economic risks of water electrolyzers. These risks can be minimized by developing precious metal-free catalysts and by diversifying catalyst material supply.[13] One strategy to develop electrocatalysts for corrosive acidic environments is to select materials with good inherent acidic stability and then tune their catalytic activity by modifying their structure. Among several transition metals, tantalum-based materials are known for their good stability under acidic media.[14] However, tantalum oxides, the most-studied Ta-based materials, are insulators in their pristine form with poor or no OER performance.[15,16]

Several efforts have been made to induce electrical conductivity and improve the OER performance of Ta_2O_5-based electrocatalysts in alkaline media. Using the pulsed laser deposition method, Xiao *et al.*[16] grew stable $Ta_2O_{5\pm d}$ nanolayers over a carbon cloth by controlling the oxygen environment. The pristine Ta_2O_5 did not have catalytic

Institut National de la Recherche Scientifique – Centre Énergie Matériaux Télécommunications, 1650 Boul. Lionel-Boulet, Varennes, J3X 1P7, Quebec, Canada. E-mail: kulbir.ghuman@inrs.ca

activity, but the O-rich Ta_2O_5 with a thickness of 8 nm showed an overpotential of 0.385 V at 10 mA cm^{-2} in a 1 M KOH solution.[16] They reported that controlling the oxygen partial pressure and keeping the thickness of the nanolayer small could enable the efficient performance of Ta_2O_5 for OER. Liu *et al.* synthesized Fe-doped O-rich Ta_2O_5 nanolayers with a thickness of about 5 nm, which showed an overpotential of 0.38 V at 10 mA cm^{-2} in the 1 M KOH solution with the optimal Fe concentration of 5 at%.[15] This work reported that doping with transition metals could increase the electrical conductivity of Ta_2O_5 and activate its surface for OER.

Yue *et al.* synthesized tantalum dioxyfluoride (TaO_2F) over graphitized carbon.[17] When TaO_2F was loaded over the carbon material with high electrical conductivity, an improvement in the charge transfer and OER performance was observed. The authors suggested that when fluorine was introduced into the TaO_2F structure, more positive charge could be distributed by Ta sites of TaO_2F compared to Ta_2O_5/CC (Cabot Vulcan XC 72R), Ta_2O_5, and $KTaO_3$, which benefited the adsorption and reaction of intermediates. So, TaO_2F loaded on graphitized carbon reached an overpotential of 0.360 V at 10 mA cm^{-2} in the alkaline medium.[17] Ruiz-Cornejo *et al.*[18] supported Ta_2O_5 over highly graphitic carbon nanofibers (CNFs), in which the sample with the lowest O/Ta (non-stoichiometric composition) led to the best OER performance in the alkaline medium. Ahmed *et al.*[19] loaded Ta_2O_5 particles over Fe_2O_3 through the hydrothermal treatment. They reported that the Fe_2O_3/Ta_2O_5 double oxide heterostructure had a low overpotential of 0.231 V in alkaline media, which was attributed to the synergistic effect and interfacial interaction between Fe_2O_3 and Ta_2O_5.[19] Ta_2O_5 is stable under OER polarization conditions in acidic media,[20] yet there have been very few studies that have explored its performance under such an environment. Mondschein *et al.*[14] fabricated polycrystalline pellets of Ni_2Ta through arc melting and molding. This material could combine the corrosion resistance of Ta and the OER activity of Ni in acidic media and achieve an overpotential of 0.570 V in 0.5 M H_2SO_4.

To develop stable and active Ta_2O_5-based electrocatalysts for OER in an acidic medium, it is crucial to identify strategies to enhance its performance and establish clear structure–property relationships. For instance, there have been inconsistent reports in the literature regarding the role of the O/Ta ratio in alkaline medium. Xiao *et al.*[16] reported better OER performance with O-rich Ta_2O_5, and Ruiz-Cornejo *et al.*[18] found that a lower O/Ta ratio results in better performance. Furthermore, while the use of carbon-based materials to improve the charge transfer with Ta_2O_5-based and NiFe alloy nanoparticles[21] electrocatalysts has been explored, their role in altering the electronic and electrocatalytic properties of Ta_2O_5 remains unexplored.

Herein, we performed density functional theory (DFT) calculations on (200), (120), and (100) Ta_2O_5 facets to identify strategies to unlock the OER performance of the Ta_2O_5 in an acidic medium. The effect of a Ta or O defect on the electronic properties of (200) and (120) facets was studied, and thirty-five different sites on facets with or without a defect were considered for OER activity evaluation. Then, correlations were identified between the OER performance and structural and electronic properties, such as Bader charge (BC), valence electrons, and DOS of Ta_2O_5 surfaces. Finally, the effect of graphene on the electronic properties and OER performance of the most active Ta_2O_5 surface was investigated.

2. Computational details

In this study, three Ta_2O_5 facets, (200), (120), and (001), reported to be stable in DFT calculations[16] and experiments,[22] were examined, as illustrated in Fig. 1A–C. The orthorhombic λ-Ta_2O_5 unit cell, with lattice parameters of a = 6.24 Å, b = 2 × 3.69 Å, and c = 3.82 Å, was used to model the surfaces.[23,24] The 200-Ta_2O_5/graphene heterostructure was also modeled with the mean absolute strain of 2.94% for graphene and Ta_2O_5, Fig. 1D. The initial distance between (200) Ta_2O_5 and graphene was changed between 2 to 5 Å to find the most stable heterostructure. As shown in Fig. S1, the model created using the initial distance of 3 Å (final distance of 3.3 Å) had the lowest total energy and was the most stable, which was considered for OER performance evaluation. To avoid interactions between periodic images, all slab models were made with a vacuum greater than 15 Å. Spin-polarized DFT calculations were performed using the Perdew–Burke–Ernzerhof (PBE) exchange–correlation functional in the generalized gradient approximation (GGA). All the DFT calculations were conducted using the Quantum Espresso software.[25] Furthermore, we utilized the DFT-D3 correction method in Grimme's scheme[26,27] for a more accurate description of the long-range van der Waals (vdW) interactions. The kinetic energy cut-off values of 35 and 350 Ry were used for wavefunctions and charge density, respectively. The energy threshold was set to 10^{-4} Ry for the self-consistent field (SCF) convergence. Davidson iterative diagonalization was employed to relax each system (without variable size) until the residual Hellman–Feynman force magnitude on each atom reached below the 10^{-3} Ry per Bohr. The DFT + U was performed to reach more accurate electronic properties. The U value of 3.66 V was taken from the Materials Project database,[28,29] as it has been used for developing Ta-based electrocatalysts in the literature.[30] The k-point sampling of 2 × 2 × 1 was used to relax the structures, and the k-point samplings of 4 × 4 × 1 and 6 × 6 × 1 were adopted for the SCF and non-self-consistent field (nSCF) calculations, respectively, to calculate the DOS and partial DOS (PDOS). The BC analysis was performed to assess the electron density of each surface.[31]

The OER performance was investigated by calculating the theoretical OER overpotential (η) according to the computational hydrogen electrode (CHE).[32] The reaction mechanism is shown in eqn (1)–(4). The following associative reaction mechanism, including four steps, was considered:

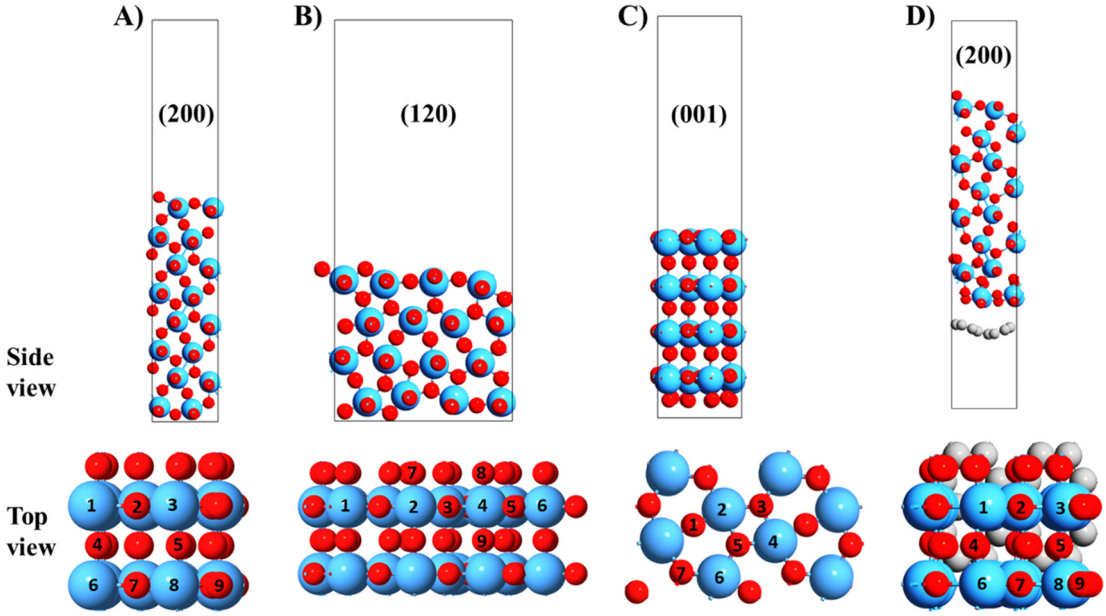

Fig. 1 The side and top views of (A) (200), (B) (120), and (C) (001) Ta_2O_5 facets, respectively. (D) The side and top views of the 200-Ta_2O_5/graphene model. The atoms with numbers in the lower panel represent the unique Ta and O sites on the surface. The O, Ta, and C atoms are represented by red, blue, and gray spheres, respectively.

$$H_2O + * \rightarrow OH^* + H^+ + e^- \quad (1)$$

$$OH^* \rightarrow O^* + H^+ + e^- \quad (2)$$

$$O^* + H_2O \rightarrow OOH^* + H^+ + e^- \quad (3)$$

$$OOH^* \rightarrow O_2 + * + H^+ + e^- \quad (4)$$

where, * indicates the surface, and O*, OH*, and OOH* refer to the adsorbed intermediates. To calculate the adsorption energy (ΔE) of each intermediate, eqn (5)–(7) were used:

$$\Delta E_{O^*} = E(O^*) - E(*) - [E(H_2O_{(g)}) - E(H_{2_{(g)}})] \quad (5)$$

$$\Delta E_{OH^*} = E(OH^*) - E(*) - [E(H_2O_{(g)}) - 0.5E(H_{2_{(g)}})] \quad (6)$$

$$\Delta E_{OOH^*} = E(OOH^*) - E(*) - [2E(H_2O_{(g)}) - 1.5E(H_{2_{(g)}})] \quad (7)$$

in these equations, $E(*)$, $E(O^*)$, $E(OH^*)$, and $E(OOH^*)$ are the total energy of the surface without adsorbates and with adsorbed intermediates of O*, OH*, and OOH*, respectively. After finding the adsorption ΔE of each intermediate, adsorption free energies ($\Delta G_{adsorption}$) were calculated according to eqn (8):

$$\Delta G_{adsorption} = \Delta E_{adsorption} + \Delta G_{correction} \quad (8)$$

For O*, OH*, and OOH*, $\Delta G_{correction}$ values (which include the contributions of zero-point energy, integrated heat capacity from 0 to 298.15 K, and entropy) of 0.044, 0.295, and 0.377 eV were used, respectively.[32] Finally, Gibbs free energy ($\Delta G_{Step\ 1\text{–}4}$) of each step at U = 0 V and OER overpotential (η) were calculated according to eqn (9)–(13):

$$\Delta G_{Step\ 1} = \Delta G_{OH^*} - \Delta G(H_2O) = \Delta G_{OH^*} - 0 = \Delta G_{OH^*} \quad (9)$$

$$\Delta G_{Step\ 2} = \Delta G_{O^*} - \Delta G_{OH^*} \quad (10)$$

$$\Delta G_{Step\ 3} = \Delta G_{OOH^*} - \Delta G_{O^*} \quad (11)$$

$$\Delta G_{Step\ 4} = \Delta G_{O_2} - \Delta G_{OOH^*} = 4.92 - \Delta G_{OOH^*} \quad (12)$$

$$\eta = \max[\Delta G_{Step\ 1}; \Delta G_{Step\ 2}; \Delta G_{Step\ 3}; \Delta G_{Step\ 4}]/e - 1.23\ V \quad (13)$$

3. Results and discussion

3.1. OER performance of pristine and defected Ta_2O_5 surfaces

First, we investigated the OER performance of various sites on pristine and defected Ta_2O_5 facets. Specifically, (200), (120), and (001) facets were investigated as they were experimentally observed and were proved to be stabilized in DFT calculations.[16] Additionally, on (200) and (120) facets, O or Ta were removed to create defected surfaces. More precisely, O5d–200-Ta_2O_5, O7d–200-Ta_2O_5, O9d–200-Ta_2O_5, Ta1d–200-Ta_2O_5, and Ta3d–200-Ta_2O_5 surfaces were modeled by removing O5, O7, O9, Ta1, and Ta3 atoms, respectively, from the pristine (200) surface (Fig. 1A). In this nomenclature, "d" indicates surfaces with an O or Ta defect. Similarly, the O5d–120-Ta_2O_5, O9d–120-Ta_2O_5, Ta4d–120-Ta_2O_5, and Ta6d–120-Ta_2O_5 surfaces were modeled by removing O5, O9, Ta4, and Ta6, respectively, from the pristine (120) surface (Fig. 1B).

The OER performance of (200) and (120) surfaces with and without defects and the pristine (001) surface is detailed in Tables S1–S3, including the ΔG values for adsorption of

reaction intermediates and steps 1–4 (eqn (9)–(12)). The defects on the (001) facet were not investigated because the pristine (001) surface showed larger overpotentials, as summarised in the SI, compared to the (200) and (120) surfaces. Fig. 2 illustrates the OER reaction pathway for Ta or Ta–O sites with overpotentials below 0.7 V.

On the pristine (200) surface, step 2 (OH* to O*) was the rate-limiting step on the Ta8–O5 bridge site, and step 3 (O* to OOH*) was the rate-limiting step on the two Ta sites (Table S1). The lowest overpotential, 0.61 V, was found on the Ta8–O5 bridge site, as illustrated in Fig. 2A. Creating oxygen defects increased the ΔG_{step4} on the O7d–, O5d–, and O9d–200-Ta_2O_5 surfaces, making oxygen desorption difficult. Therefore, step 4 became rate limiting on most sites of oxygen-deficient (200) surface. In contrast, the Ta1 site on the Ta3d–200-Ta_2O_5 surface had the lowest overpotential of 0.63 V (step 3), outperforming other single Ta sites on both pristine and O/Ta-defected surfaces.

On pristine (120), step 2 or step 3 was the rate-limiting step for Ta and Ta–O bridge sites, and the lowest overpotential was found on the Ta1 site (0.68 V, Fig. 2B). Oxygen defects in O5d– and O9d–120-Ta_2O_5 surfaces increased the ΔG_{Step4}, deteriorating the OER performance (Table S2). An overpotential of 0.76 V was found for the Ta2 site on the Ta6d–120-Ta_2O_5 surface, which compared favorably with respect to the similar site on the pristine (120) facet (1.03 V) and the Ta4d–120-Ta_2O_5 (1.22 V) surfaces.

The pristine (001) surface had the poorest performance (overpotentials above 1.8 V) compared to both (120) and (200) surfaces. On this surface, the conversion of O* to OOH* (step 3) limited the reaction (Table S3).

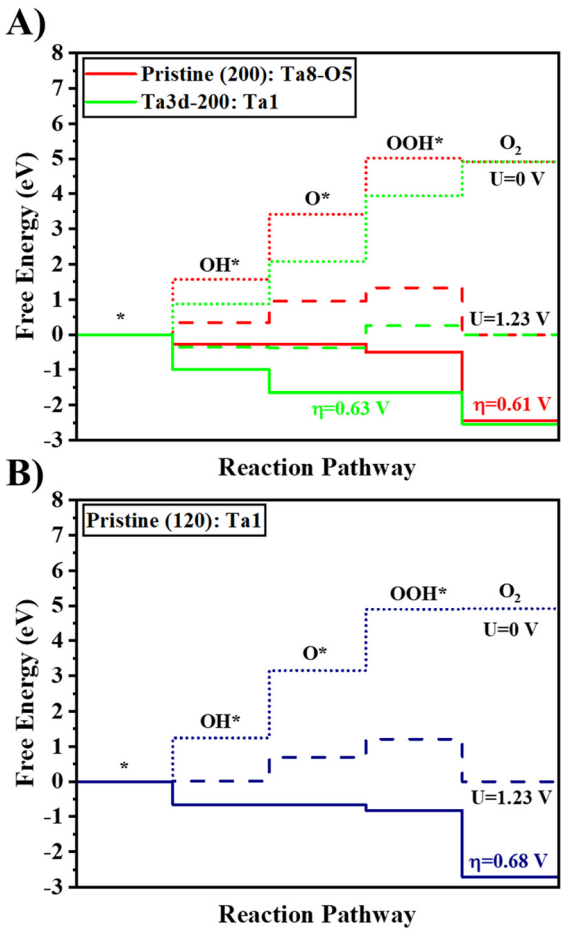

Fig. 2 Free energy diagrams for A) the Ta8–O5 bridge on the pristine (200) surface, the Ta1 site on the Ta3d–200-Ta_2O_5 surface, and B) the Ta1 site on the pristine (120) surface. The dotted, dashed, and straight lines indicate the free energy diagrams at potentials of 0, 1.23 V, and the overpotential at which OER becomes downward, respectively.

3.2. OER performance of 200-Ta_2O_5/graphene heterostructure

In practical applications, a conductive phase is added to insulating electrocatalysts to facilitate electron transport through the electrode;[16–18,33] hence, we modeled a Ta_2O_5/graphene heterostructure and investigated its OER performance. The (200) surface was considered for this heterostructure, Fig. 1D, as it showed the highest OER activity. One Ta site and three Ta–O bridge sites were investigated. The OER performance parameters ($\Delta G_{Steps\ 1–4}$, ΔG of reaction intermediates (OH*, O*, and OOH*)) and overpotential of different sites on 200-Ta_2O_5/graphene heterostructure are summarized in Table S4. Fig. 3A presents the energy diagrams for Ta6–O7 and Ta6 sites, the best-performing ones with an overpotential of 0.39 and 0.45 V, respectively. The energy diagram of the Ta6 site of 200-Ta_2O_5/graphene and of pristine (200) are further compared in Fig. 3B. As indicated in the figure, the overpotential of 1.07 V on the pristine surface decreased significantly to 0.45 V on the heterostructure. This is similar to our previous study, where adding graphene decreased the OER overpotential of Nb_2C MXene.[34]

The scaling relationship for ΔG_{OOH^*} *vs.* ΔG_{OH^*} is plotted in Fig. 4, showing a linear correlation for most sites. According to the figure, some sites, including Ta sites on O-defected (120) and O-defected (200) surfaces, exhibited strong adsorption of intermediates, which increased the overpotential, as presented in Tables S1 and S2. In contrast, the intermediates were weakly adsorbed on some sites, such as Ta sites of pristine (120) and pristine (200). Since 200-Ta_2O_5/graphene heterostructure showed the lowest overpotential, it can be stated that it possessed comparatively optimum adsorption ΔG of OOH* and OH*. This figure showed $\Delta G_{OOH^*} = (0.90715 \pm 0.13051)\Delta G_{OH^*} + (3.29035 \pm 0.1922)$, which is close to the reports in the literature.[32,35] The nearly linear relationship, with a slope close to 1, indicates that *OOH and *OH bind to the surface in a similar, single-bonded adsorption mode.[36,37]

3.3. Analysis of Ta_2O_5 facets with or without a defect

This section deciphers the reasons behind the distinct performances of the facets. Since the geometry of different facets can affect the electrocatalytic performance,[38] the compactness of each pristine facet was analyzed, as explained in SI. The surface compactness of the (001) and (200) facets (the topmost atoms) is 0.21 atom per $Å^2$, and that of the (120)

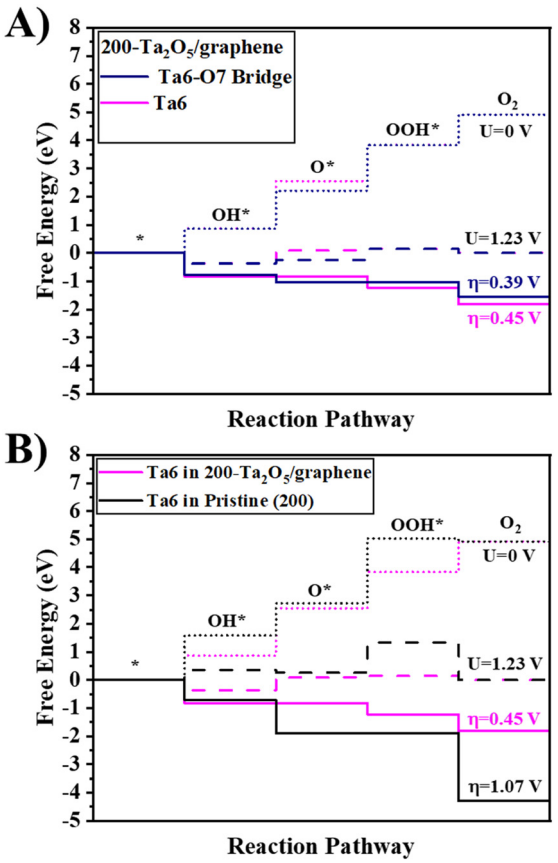

Fig. 3 A) The reaction pathway Ta6–O7 and Ta6 sites on 200-Ta_2O_5/graphene. B) Comparing the reaction pathway of the Ta6 site on 200-Ta_2O_5/graphene and pristine (200) Ta_2O_5. The dotted, dashed, and straight lines indicate the free energy diagrams at potentials of 0, 1.23 V, and the overpotential at which OER becomes downward, respectively.

surface is 0.23 atom per Å^2. Moreover, the density of Ta atoms on the layers of the (001), (120), and (200) facets is 0.087, 0.072, and 0.071 Ta atoms per Å^2, respectively. Thus, the trend of OER performance for these surfaces followed the Ta density on the facets: the (001) facet with the highest Ta density shows the highest overpotentials (between 1.8 and 3.5 V, Table S3). Instead, on the other facets with lower Ta density, the overpotentials were below 1.1 V for the pristine (200) (Table S1) and between 0.68 and 2.0 V for most sites (except one with 2.6 V, Table S2) on the pristine (120) facet. This result is similar to RuO_2, where the (111) facet with the lowest active site density had the lowest overpotential of 0.35 V, and the (101) facet with the highest active site density had the highest overpotential of 0.60 V.[39]

Fig. 5 compares the DOS curves of the pristine facets. It shows that the (001) and (200) facets do not have a bandgap, but the former has higher DOS at the Fermi level compared to the latter. Instead, the (120) facet has a band gap, indicating an insulating behavior. The Fermi-level electrons can increase the likelihood of electron transfer to reaction intermediates.[40,41] In the (200) facet, the DOS at the Fermi level was intermediate between the (001) and (120) facets, which may explain its better OER performance. This balance enables the optimal electronic contribution to the intermediates – neither too high (strongly adsorbing intermediates) nor too low (weakly adsorbing intermediates) – that can facilitate the efficient bonding and electron transfer between the surface and intermediates.

The total DOS analysis of (120) surfaces without and with Ta or O defects are compared in Fig. S2A. In the pristine (120), the Fermi level is closer to the valence band (VB) edge.

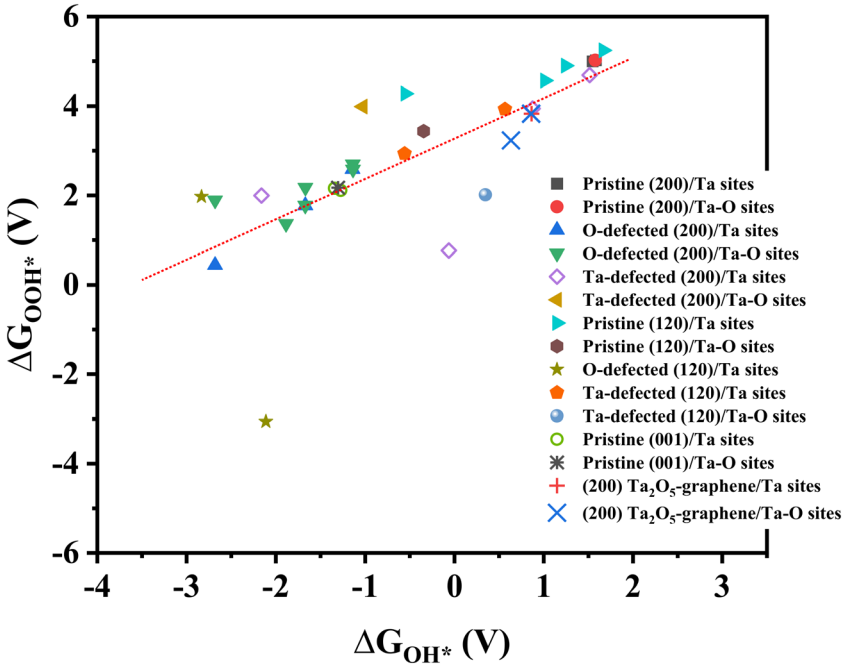

Fig. 4 Scaling relationships of adsorption ΔG of OOH* *vs.* OH* for all Ta and Ta–O sites on all facets with or without a defect.

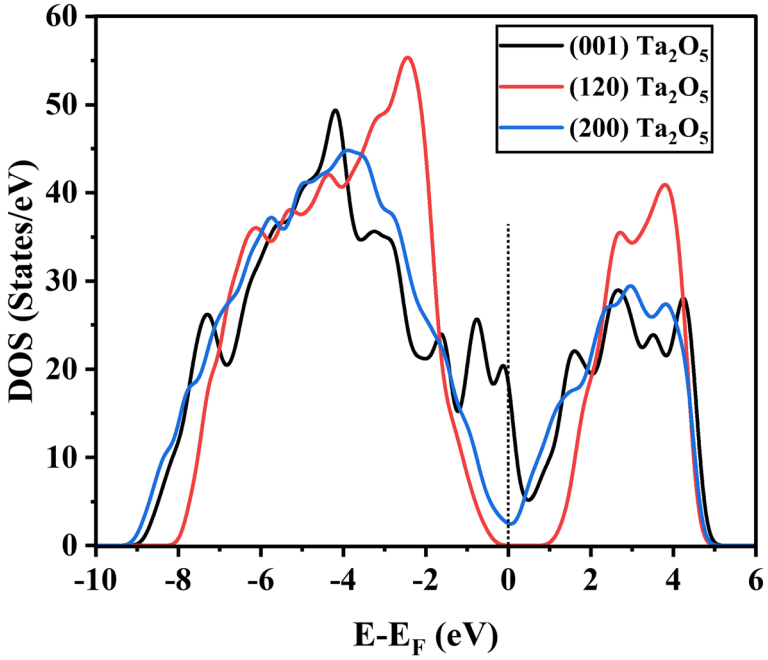

Fig. 5 Comparing the DOS curves of pristine (001), (120), and (200) surfaces.

In O5d– and O9d–120-Ta_2O_5 surfaces, creating O defects shifted the VB states away from the Fermi level and placed the Fermi level in the conduction band (CB). This shows the formation of the n-type semiconductor. In contrast, creating Ta defects, as in Ta6d– and Ta4d–120-Ta_2O_5, shifted the Fermi level into the VB states, indicating the formation of a p-type semiconductor.[42]

The total DOS analysis of the (200) surface with and without defects is shown in Fig. S3A. Creating Ta defects on this surface did not introduce a bandgap, keeping its metallic nature. In the (200) surface with the Ta defect, the Fermi level was located inside the VB. However, the O defects created a bandgap and shifted the Fermi level inside the CB, exhibiting n-type semiconductor behavior. This trend was similar to the (120) facet with a Ta or O defect. This is significant because reducing the (200) surface may lead to a decrease in the electrical conductivity.

3.4. Analysis of the varied OER performance of different Ta sites

In addition to the electronic and geometrical analysis of the pristine and defective facets, all unique Ta sites were screened individually. To this end, the PDOS curves of (120) and (200) facets were plotted, and the d orbitals of each Ta site were compared since they can significantly affect the catalytic activity.[43–45] Then, the PDOS width at the Fermi level, the maximum PDOS width in the valence band (MPWV) and its position,[46] maximum PDOS width in the conduction band (MPWC) and its position, valence band maxima (VBM), and conduction band minima (CBM) of the d orbitals were extracted. The schematic representation of parameters derived from d orbitals of single Ta sites is shown in Fig. S5. Moreover, the BC of the Ta sites and the nearest atom, and the sum of valence electrons (SVE) within 2 and 3 Å radii were calculated. Finally, heatmaps for (120) and (200) surfaces are provided in Fig. 6 and 8, respectively, to highlight possible correlations between the OER performance ($\Delta G_{\text{Steps 1–4}}$, $\Delta G_{\text{OH*}}$, $\Delta G_{\text{O*}}$, $\Delta G_{\text{OOH*}}$, overpotential) and the properties of each Ta site.

3.4.1. Properties of Ta sites on the (120) Ta_2O_5 surface. The PDOS analysis of d orbitals of the Ta sites on the (120) surface with and without defects is shown in Fig. S2B. As expected, the same trends as with the total DOS analysis were found: creating O or Ta defects shifted the Fermi level to inside the CB and VB, respectively. The heatmap in Fig. 6 shows the interdependence between properties of each Ta site (data derived from d orbitals, BC, and SVE within the radii of 2 and 3 Å) with OER performance metrics for this surface, which was calculated using Pearson's correlation coefficient analysis.[47] Notably, heatmaps show the relationship between different parameters, and they cannot be extended to features and data that are not included in our calculations.

Significant correlations were found between the properties of Ta d orbitals and OER performance metrics. MPWV showed strong correlations with $\Delta G_{\text{Step 2}}$, $\Delta G_{\text{Step 4}}$, $\Delta G_{\text{O*}}$, and $\Delta G_{\text{OOH*}}$, with its position also playing a significant role, as seen in Fig. 6 and 7. The higher the MPWV, the higher the contribution of valence electrons to the reaction, and its position can control the hybridization between reaction intermediates and the active site. An increase in the MPWV could decrease $\Delta G_{\text{Step 2}}$ and increase $\Delta G_{\text{Step 4}}$, suggesting that a higher electron presence might hinder the oxygen desorption step. The MPWV position

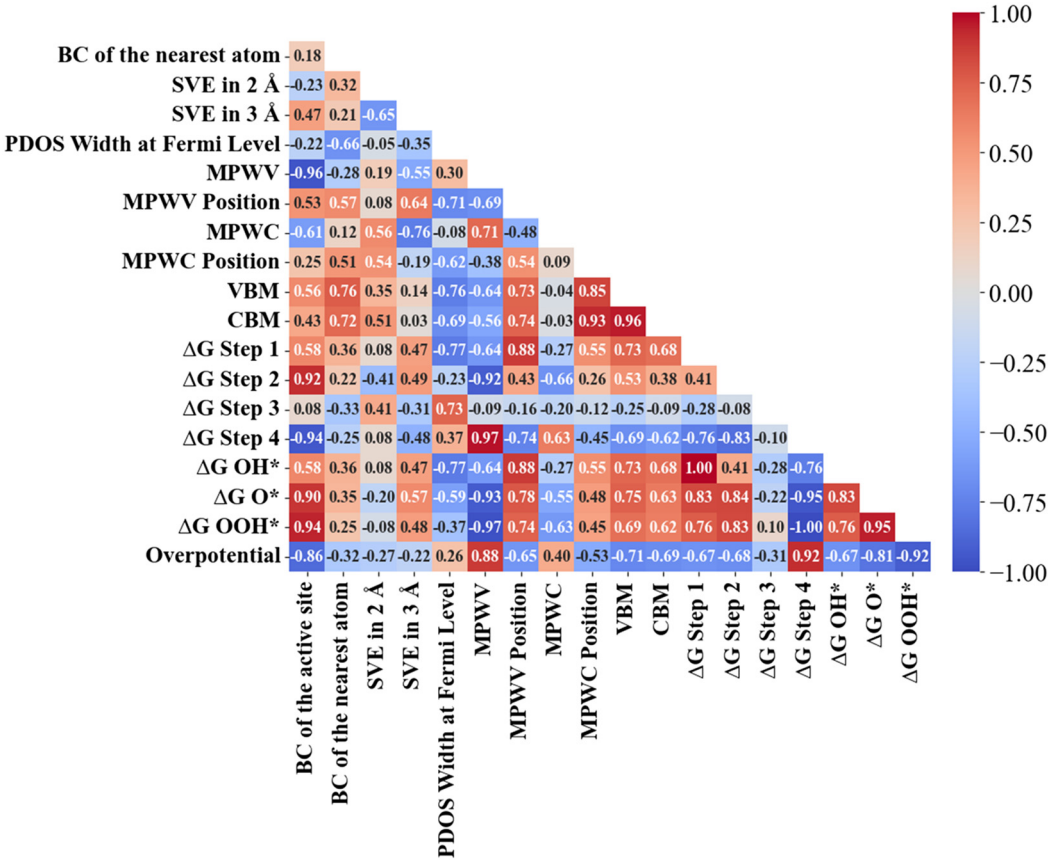

Fig. 6 Correlations between the OER performance metrics ($\Delta G_{Step1-4}$, ΔG_{OH*}, ΔG_{O*}, ΔG_{OOH*}, and overpotential) and Bader charge (BC) of the active site and its nearest neighboring atom, the sum of valence electrons (SVE) within 2 and 3 Å radii, the PDOS width at Fermi level, the maximum PDOS width in the valence band (MPWV) and its position, maximum PDOS width in the conduction band (MPWC) and its position, the valence band maxima (VBM), and conduction band minima (CBM) for Ta sites on the (120) facet with and without defects.

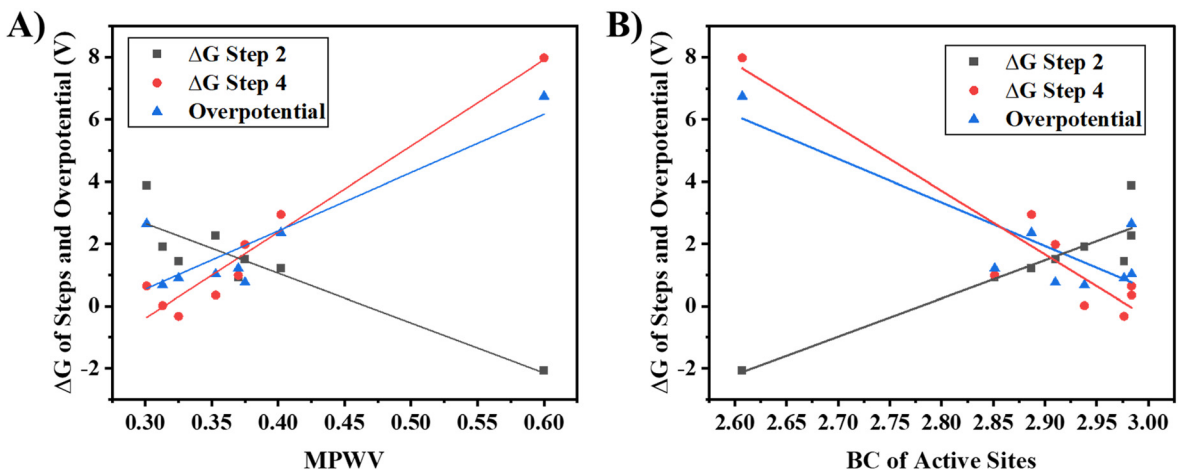

Fig. 7 The relation between $\Delta G_{Steps\ 2\&4}$ and overpotential and (A) MPWV and (B) BC of eight Ta sites for the (120) surfaces with and without defects.

had a correlation of −0.74 with $\Delta G_{Step\ 4}$, indicating that shifting the MPWV closer to the Fermi level can decrease $\Delta G_{Step\ 4}$, thereby facilitating the oxygen desorption step. In addition, MPWV had the strongest correlation (0.88) with overpotential. The heatmap also reveals that MPWC and its position had moderate correlations with OER performance metrics. Interestingly, $\Delta G_{Step\ 3}$ (O* to OOH*) only correlated with the PDOS width at the Fermi level, 0.73, showing that the increase

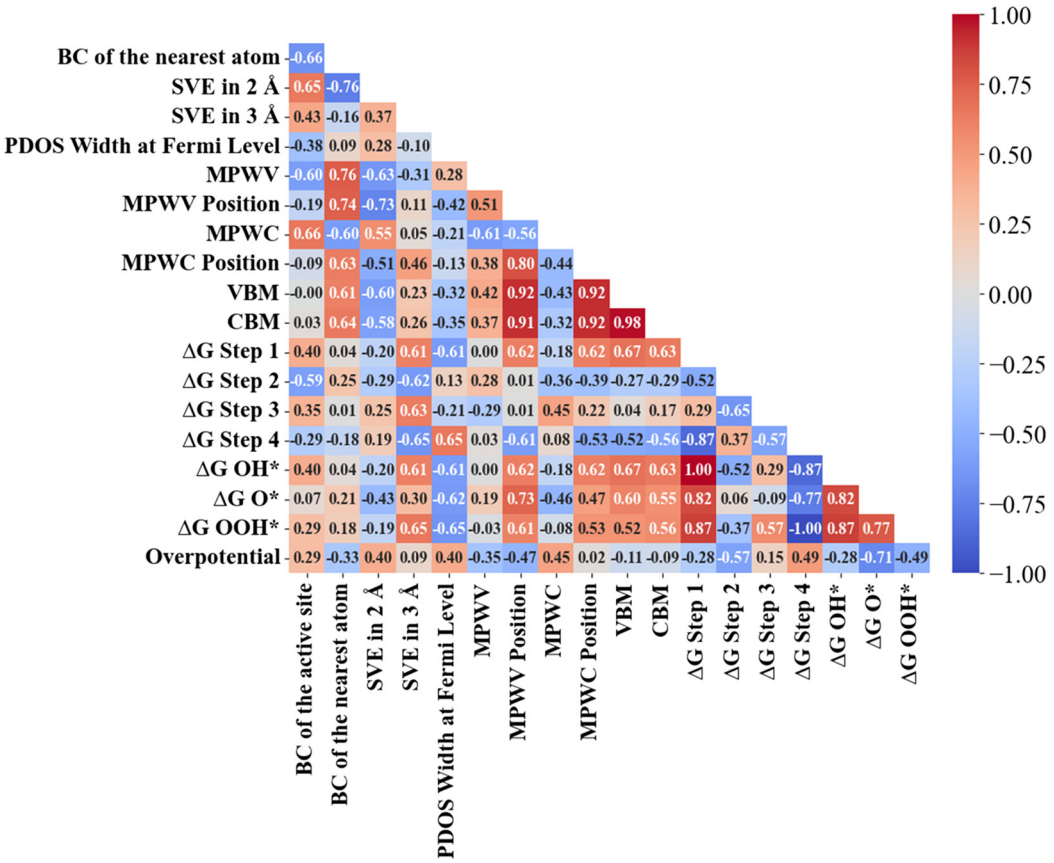

Fig. 8 Correlations between the OER performance metrics ($\Delta G_{Step1-4}$, ΔG_{OH*}, ΔG_{O*}, $\Delta G_{OOH}*$, and overpotential) and Bader charge (BC) of the active site and its nearest neighboring atom, the sum of valence electrons (SVE) within 2 and 3 Å radii, the PDOS width at Fermi level, the maximum PDOS width in the valence band (MPWV) and its position, maximum PDOS width in the conduction band (MPWC) and its position, the valence band maxima (VBM), and conduction band minima (CBM) for Ta sites on the (200) facet with and without defects.

in Fermi-level electrons can increase $\Delta G_{Step\ 3}$. The role of DOS width at the Fermi level in OER has been observed in the literature,[48] where the increase in the DOS at the Fermi level decreased the adsorption energy gap between O* and OOH*.[48]

The BC of Ta sites (Fig. 6 and 7B) strongly correlated with ΔG_{O*} and ΔG_{OOH*}, and with $\Delta G_{Step\ 2}$ and $\Delta G_{Step\ 4}$. Notably, while increasing the BC increased ΔG_{O*} and $\Delta G_{Step\ 2}$ (OH* to O*), it simultaneously reduced $\Delta G_{Step\ 4}$ (the oxygen desorption step). Therefore, a higher BC does not necessarily enhance OER performance. However, increasing the BC of Ta sites can improve the OER performance for sites where step 4 is rate-limiting. Moreover, a strong negative correlation of −0.86 was found between the BC of Ta atoms and the OER overpotential, which is in line with the literature showing the strong effect of BC on the OER activity of various materials.[49–52] The negative correlation suggests that a decrease in BC (*i.e.*, lower positive charge on the Ta sites) leads to an increase in overpotential. It should be noted that BC of the nearest O atoms and SVE within 2 and 3 Å radii of Ta sites had no significant effect on the OER performance.

3.4.2. Properties of Ta sites on the (200) Ta_2O_5 surface. The PDOS analysis of the Ta d orbitals of the (200) surface with and without a defect is shown in Fig. S3B. Similar to the (120) surfaces with O defects, the Fermi level was in the CB, and the reverse was found for structures having Ta defects. Moreover, as shown in Fig. S3B, the d orbital of Ta atoms on the pristine (200) facet did not significantly contribute to the PDOS at the Fermi level, where the p orbital of oxygen sites dominated.

The correlation heatmap of the (200) surface with and without defects is shown in Fig. 8. In contrast to 120-Ta_2O_5 surfaces, (200) surfaces did not have strong correlations with the properties of Ta sites. This again indicates a significant facet-dependent behavior of Ta_2O_5 for OER, similar to other materials such as IrO_2 and Co-based electrocatalysts.[39,53,54]

A moderate correlation was observed between the BC and $\Delta G_{Step\ 2}$ (−0.59) and between the SVE within a 3 Å radius and $\Delta G_{Step\ 1-4}$, ΔG_{OH*}, and $\Delta G_{OOH}*$. This suggests that the presence of valence electrons at a longer range (3 Å) is more influential in modulating the reaction than at a shorter range (2 Å). Moreover, the PDOS width at the Fermi level had correlations of −0.61 to −0.65 with ΔG_{OH*}, ΔG_{O*}, and ΔG_{OOH*}. This implies that a higher density of electrons at the Fermi level could decrease the ΔG of all intermediates and increase $\Delta G_{Step\ 4}$. Similar results have been found,[55] for instance, between the adsorption energy of O_2 and DOS width at the Fermi level for N-doped graphdiyne.[56]

3.5. The 200-Ta_2O_5/graphene heterostructure

Here, the effect of graphene on the electronic properties and OER performance of the (200) Ta_2O_5 facet is discussed. Fig. 9A compares the total DOS curves of 200-Ta_2O_5/graphene and (200) Ta_2O_5. The major difference is the higher intensity of the DOS curve in the VB and CB in the 200-Ta_2O_5/graphene structure, which can improve the orbital hybridization level between the surface and reaction intermediates. In addition, the DOS width at the Fermi level was reduced after adding graphene, which indicates the lower capability of the surface in transferring electrons to intermediates. To analyze this further, we compared the PDOS curve of O and C p orbitals and Ta d orbitals in the heterostructure and O p and Ta d orbitals in (200) Ta_2O_5, as shown in Fig. 9B. Regarding the O p orbitals, the PDOS intensity in the VB and CB was increased after adding graphene. However, the O p orbitals of the (200) surface contributed more at the Fermi level compared to that of the 200-Ta_2O_5/graphene heterostructure. The PDOS intensity of Ta d orbitals in the VB and CB for the 200-Ta_2O_5/graphene was higher than that of the pristine (200) surface. This leads to higher valence electron contribution of Ta sites of 200-Ta_2O_5/graphene during the reaction (stronger hybridization), which might explain the better performance of Ta sites after adding graphene. In addition, the C p orbitals in the heterostructure overlapped with Ta d orbitals in the VB in the range of −8 to −4 eV.

Fig. 9C compares the PDOS curves of d orbitals of the Ta6 site over 200-Ta_2O_5/graphene and pristine (200). The MPWV and MPWC in the 200-Ta_2O_5/graphene were higher, and their position shifted toward lower energies. As a result, the Ta6 sites over pristine (200) and 200-Ta_2O_5/graphene surfaces had overpotentials of 0.91 and 0.46 V, respectively, where the rate-limiting step was steps 3 and 2. This can be attributed to the higher PDOS intensity of the d orbital in the VB after adding graphene, which increased $\Delta G_{\text{step 4}}$ from −0.08 to 1.09 V and decreased $\Delta G_{\text{step 3}}$ from 2.14 to 1.28 V. Based on the results, it is clear that the changes in the intensity of d orbitals of Ta sites in heterostructure lead to significant differences in performances. Notably, an oxygen atom was close to Ta8 on the 200-Ta_2O_5/graphene surface, so we could not evaluate a single Ta8 site since the adsorbates were interacting with both Ta and O in this case.

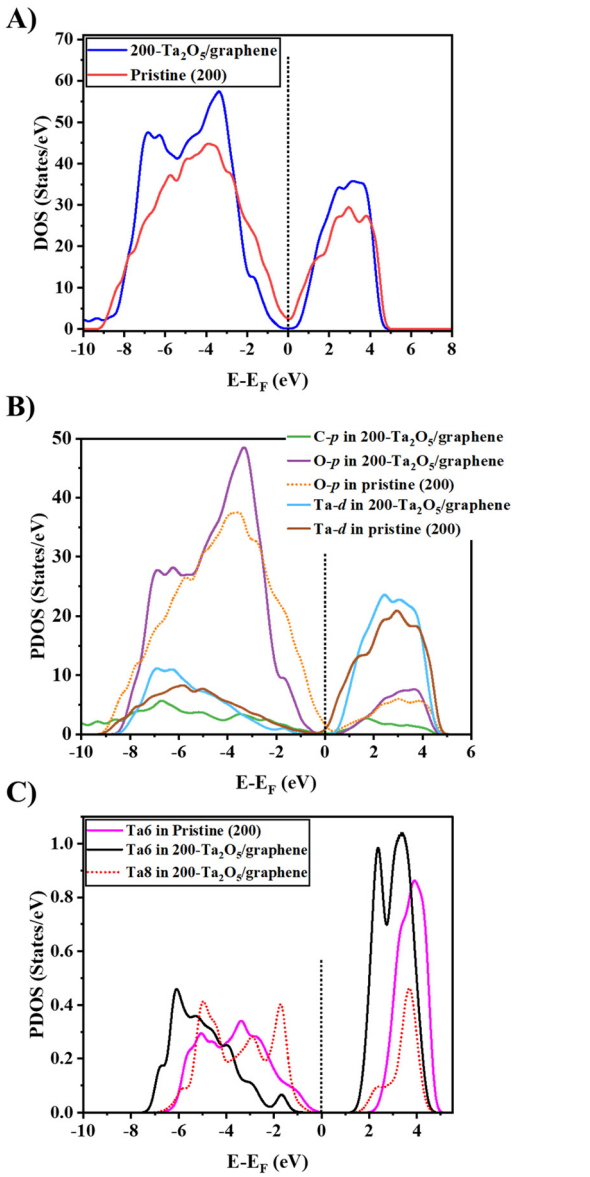

Fig. 9 A) Comparing the DOS of 200-Ta_2O_5/graphene and pristine (200) Ta_2O_5. B) Comparing the PDOS analysis of C and O p orbitals and Ta d orbital of 200-Ta_2O_5/graphene and pristine (200) Ta_2O_5, respectively. C) PDOS analysis of the d orbital of the Ta6 site on 200-Ta_2O_5/graphene and pristine (200) Ta_2O_5. D) PDOS analysis of p and d orbitals of active O and Ta sites on 200-Ta_2O_5/graphene.

4. Conclusion

In this work, DFT calculations were performed on the (200), (120), and (001) surfaces of Ta_2O_5 and on the 200-Ta_2O_5/graphene heterostructure to identify strategies to enhance the OER performance of Ta_2O_5. New insights into the OER activity of Ta sites on pristine facets were established. The (200) facet, with the lowest Ta site density and moderate DOS at the Fermi level, showed the lowest overpotential compared to the (120) and (001) facets. Creating Ta defects could decrease the overpotential of a Ta site on the (200) and (120) facets. However, creating O defects created a bandgap in the (200) facet and increased the overpotential on (200) and (120) facets. Correlation heatmaps were established between properties of each Ta site on the (200) and (120) facets and the OER performance metrics. On the second best-performing facet, the (120), the Bader charge and d orbitals of Ta sites at the VB significantly modulated the performance, correlating strongly with the Gibbs free energy (ΔG) of steps 1, 2, and 4. However, on the (200) facet, only SVE within 3 Å and PDOS width at the Fermi level exhibited moderate correlations. The 200-Ta_2O_5/graphene heterostructure showed a substantially low overpotential of 0.39 V on a Ta–O site. The PDOS analysis

showed that the improved OER performance of the heterostructure was due to the shift of the d orbitals of Ta sites toward lower energies and the increase in the DOS intensity after adding graphene. Overall, the best strategies to unlock the potential of Ta oxide in OER is to synthesize a heterostructure formed by (200) Ta_2O_5 and graphene, prevent the formation of the (001) facet, and/or create Ta defects in Ta_2O_5 nanoparticles or thin films. If validated in experiments, these results would conduce to Ta_2O_5-based materials as promising non-precious OER electrocatalysts under acidic media.

Author contributions

Ebrahim Ghasemy: data curation, investigation, methodology, visualization, and writing – original draft, and writing – review & editing. Ana C. Tavares: conceptualization, project administration, supervision, funding acquisition, writing – review & editing. Kulbir Kaur Ghuman: conceptualization, funding acquisition, investigation, methodology, project administration, supervision, writing – review & editing.

Conflicts of interest

The authors declare the following financial interests/personal relationships, which may be considered potential competing interests: Kulbir K. Ghuman and Ana C. Tavares report that financial support was provided by the Natural Sciences and Engineering Research Council of Canada. Kulbir K. Ghuman and Ana C. Tavares report that financial support was provided by PRIMA Quebec. Kulbir K. Ghuman and Ana C. Tavares report that financial support was provided by Niobay Metals Inc. If there are other authors, they declare that they have no known competing financial interests or personal relationships that could have appeared to influence the work reported in this paper.

Data availability

Supplementary information is available. See DOI: **https://doi.org/10.1039/D5LF00195A**.

The structural model of Ta_2O_5 used in this study was based on the structural coordinates from Lee, S. H., Kim, J., Kim, S. J., Kim, S., & Park, G. S. (2013), Hidden structural order in orthorhombic Ta_2O_5, *Physical Review Letters*, 110(23), 235–502. (**https://doi.org/10.1103/PhysRevLett.110.235502**).

No new experimental data were generated.

Acknowledgements

The authors acknowledge the Natural Sciences and Engineering Research Council of Canada (NSERC) Discovery grant program [RGPIN-2020-05924; RGPIN-2020-05950], NSERC Alliance program [576728-2022], PRIMA Québec [R24-13-001-PME], Canada Research Chair (CRC) program [CRC-2019-00231], and the Canada Foundation for Innovation (CFI) for infrastructure and operating funds. This research was enabled by computational resources provided by Calcul Québec (**https://www.calculquebec.ca**) and Digital Research Alliance of Canada (**https://www.alliancecan.ca**). The authors would also like to thank Niobay for their financial support.

References

1 G. A. Reigstad, S. Roussanaly, J. Straus, R. Anantharaman, R. de Kler, M. Akhurst, N. Sunny, W. Goldthorpe, L. Avignon and J. Pearce, *Adv. Appl. Energy*, 2022, **8**, 100108.
2 S. F. Ahmed, M. Mofijur, S. Nuzhat, N. Rafa, A. Musharrat, S. S. Lam and A. Boretti, *Int. J. Hydrogen Energy*, 2021, **47**, 37227–37255.
3 M. M. Aba, I. L. Sauer and N. B. Amado, *Int. J. Hydrogen Energy*, 2024, **57**, 660–678.
4 Hydrogen Strategy for Canada: Seizing the Opportunities for Hydrogen, **https://publications.gc.ca/site/eng/9.894114/publication.html**.
5 S. S. Kumar and H. Lim, *Energy Rep.*, 2022, **8**, 13793–13813.
6 H. Ishaq, I. Dincer and C. Crawford, *Int. J. Hydrogen Energy*, 2022, **47**, 26238–26264.
7 Z. Chen, X. Duan, W. Wei, S. Wang and B.-J. Ni, *Nano Energy*, 2020, **78**, 105392.
8 Z. P. Wu, X. F. Lu, S. Q. Zang and X. W. Lou, *Adv. Funct. Mater.*, 2020, **30**, 1910274.
9 K. Wang, X. Wang, Z. Li, B. Yang, M. Ling, X. Gao, J. Lu, Q. Shi, L. Lei and G. Wu, *Nano Energy*, 2020, **77**, 105162.
10 S. Kaushik, X. Xiao and Q. Xu, *EnergyChem*, 2023, **5**, 100104.
11 A. Goñi-Urtiaga, D. Presvytes and K. Scott, *Int. J. Hydrogen Energy*, 2012, **37**, 3358–3372.
12 H. Wu, Y. Wang, Z. Shi, X. Wang, J. Yang, M. Xiao, J. Ge, W. Xing and C. Liu, *J. Mater. Chem. A*, 2022, **10**, 13170–13189.
13 M. A. Hubert, L. A. King and T. F. Jaramillo, *ACS Energy Lett.*, 2021, **7**, 17–23.
14 J. S. Mondschein, K. Kumar, C. F. Holder, K. Seth, H. Kim and R. E. Schaak, *Inorg. Chem.*, 2018, **57**, 6010–6015.
15 A. Liu, Z. Chen, X. Wei, W. Xiao and J. Ding, *MRS Commun.*, 2017, **7**, 563–569.
16 W. Xiao, X. Huang, W. Song, Y. Yang, T. S. Herng, J. M. Xue, Y. P. Feng and J. Ding, *Nano Energy*, 2016, **25**, 60–67.
17 X. Yue, Y. Jin and P. K. Shen, *J. Mater. Chem. A*, 2017, **5**, 8287–8291.
18 J. C. Ruiz-Cornejo, J. F. Vivo-Vilches, D. Sebastián, M. V. Martínez-Huerta and M. J. Lázaro, *Renewable Energy*, 2021, **178**, 307–317.
19 I. Ahmed, V. Burman, R. Biswas, A. Roy, R. Sharma and K. K. Haldar, *New J. Chem.*, 2023, **47**, 17284–17292.
20 Z. Wang, X. Guo, J. Montoya and J. K. Nørskov, *npj Comput. Mater.*, 2020, **6**, 160.
21 M. Zhao, H. Li, W. Yuan and C. M. Li, *ACS Appl. Energy Mater.*, 2020, **3**, 3966–3977.
22 S. Boughaba, G. Sproule, J. McCaffrey, M. Islam and M. Graham, *Thin Solid Films*, 2000, **358**, 104–113.
23 J.-H. Hur, *Comput. Mater. Sci.*, 2019, **164**, 17–21.
24 S.-H. Lee, J. Kim, S.-J. Kim, S. Kim and G.-S. Park, *Phys. Rev. Lett.*, 2013, **110**, 235502.

25 J. P. Perdew, K. Burke and M. Ernzerhof, *Phys. Rev. Lett.*, 1996, **77**, 3865.
26 S. Grimme, J. Antony, S. Ehrlich and H. Krieg, *J. Chem. Phys.*, 2010, **132**, 154104.
27 S. Grimme, S. Ehrlich and L. Goerigk, *J. Comput. Chem.*, 2011, **32**, 1456–1465.
28 L. Wang, T. Maxisch and G. Ceder, *Phys. Rev. B: Condens. Matter Mater. Phys.*, 2006, **73**, 195107.
29 A. Jain, G. Hautier, S. P. Ong, C. J. Moore, C. C. Fischer, K. A. Persson and G. Ceder, *Phys. Rev. B: Condens. Matter Mater. Phys.*, 2011, **84**, 045115.
30 S. Back, A. H. B. Mostaghimi and S. Siahrostami, *ChemCatChem*, 2022, **14**, e202101763.
31 G. Henkelman, A. Arnaldsson and H. Jónsson, *Comput. Mater. Sci.*, 2006, **36**, 354–360.
32 G. K. K. Gunasooriya and J. K. Nørskov, *ACS Energy Lett.*, 2020, **5**, 3778–3787.
33 X. Miao, Z. Peng, L. Shi and S. Zhou, *ACS Catal.*, 2023, **13**, 3983–3989.
34 P. Schütt, E. Ghasemy, A. C. Tavares and K. K. Ghuman, *ACS Appl. Nano Mater.*, 2023, **6**, 21829–21838.
35 S. Back, K. Tran and Z. W. Ulissi, *ACS Catal.*, 2019, **9**, 7651–7659.
36 J. Zhang, H. B. Tao, M. Kuang, H. B. Yang, W. Cai, Q. Yan, Q. Mao and B. Liu, *ACS Catal.*, 2020, **10**, 8597–8610.
37 J. Feng, Z. Dong, Y. Ji and Y. Li, *JACS Au*, 2023, **3**, 1131–1140.
38 J. Solla-Gullon, F. Vidal-Iglesias and J. Feliu, *Annu. Rep. Prog. Chem., Sect. C: Phys. Chem.*, 2011, **107**, 263–297.
39 S. Saha, P. Gayen and V. K. Ramani, *ChemCatChem*, 2020, **12**, 4922–4929.
40 N. Soin, S. S. Roy, T. H. Lim and J. A. McLaughlin, *Mater. Chem. Phys.*, 2011, **129**, 1051–1057.
41 L. Ji, S. Yu, X. Zhou, Y. Bao, F. Yang, W. Kang and X. Zhang, *Anal. Chim. Acta*, 2019, **1079**, 86–93.
42 P. Rastogi, S. Kumar, S. Bhowmick, A. Agarwal and Y. S. Chauhan, *J. Phys. Chem. C*, 2014, **118**, 30309–30314.
43 N. Ma, Y. Zhang, Y. Wang, J. Zhao, B. Liang, Y. Xiong, S. Luo, C. Huang and J. Fan, *J. Colloid Interface Sci.*, 2024, **654**, 1458–1468.
44 H. Xin, A. Vojvodic, J. Voss, J. K. Nørskov and F. Abild-Pedersen, *Phys. Rev. B: Condens. Matter Mater. Phys.*, 2014, **89**, 115114.
45 H. Xin and S. Linic, *J. Chem. Phys.*, 2010, **132**, 221101.
46 Y. Jiao, Y. Zheng, K. Davey and S.-Z. Qiao, *Nat. Energy*, 2016, **1**, 1–9.
47 I. Cohen, Y. Huang, J. Chen, J. Benesty, J. Benesty, J. Chen, Y. Huang and I. Cohen, *Noise Reduction in Speech Processing*, 2009, pp. 1–4.
48 L. Wang, Q. Zhou, Z. Pu, Q. Zhang, X. Mu, H. Jing, S. Liu, C. Chen and S. Mu, *Nano Energy*, 2018, **53**, 270–276.
49 Z. Fu, G. Hai, X.-X. Ma, D. Legut, Y. Zheng and X. Chen, *J. Energy Chem.*, 2024, **98**, 663–669.
50 C. Yang, Y. Wu, Y. Wang, H.-N. Zhang, L.-H. Zhu and X.-C. Wang, *Nanoscale*, 2022, **14**, 187–195.
51 Y. Zhou, L. Sheng, L. Chen, W. Zhang and J. Yang, *J. Phys. Chem. Lett.*, 2024, **15**, 11454–11461.
52 Z. Zhang, G. Tan, A. Kumar, H. Liu, X. Yang, W. Gao, L. Bai, H. Chang, Y. Kuang and Y. Li, *Mol. Catal.*, 2023, **535**, 112852.
53 S. Kwon, K. A. Stoerzinger, R. Rao, L. Qiao, W. A. Goddard III and Y. Shao-Horn, *J. Am. Chem. Soc.*, 2024, **146**, 11719–11725.
54 E. M. Davis, A. Bergmann, H. Kuhlenbeck and B. Roldan Cuenya, *J. Am. Chem. Soc.*, 2024, **146**, 13770–13782.
55 D. Pan, Q. Liu, F. Nichols, R. Mercado, H.-L. Kuo, J. Q. Lu, F. Bridges and S. Chen, *J. Colloid Interface Sci.*, 2023, **629**, 591–597.
56 Y. Wang, T. N. Pham, H. H. Halim, L. Yan and Y. Morikawa, *Mater. Adv.*, 2023, **4**, 6542–6552.